Faraday Discussions

Cite this: *Faraday Discuss.*, 2015, **184**, 101

PAPER

Single occupancy spectroelectrochemistry of freely diffusing flavin mononucleotide in zero-dimensional nanophotonic structures

Lawrence P. Zaino, III†[a] Dane A. Grismer,†[b] Donghoon Han,[b] Garrison M. Crouch[b] and Paul W. Bohn*[ab]

Received 11th May 2015, Accepted 1st July 2015
DOI: 10.1039/c5fd00072f

Zero-mode waveguides (ZMW) have the potential to be powerful confinement tools for studying electron transfer dynamics at single molecule occupancy conditions. Flavin mononucleotide contains an isoalloxazine chromophore, which is fluorescent in the oxidized state (FMN) while the reduced state ($FMNH_2$) exhibits dramatically lower light emission, *i.e.* a dark-state. This allows fluorescence emission to report the redox state of single FMN molecules, an observation that has been used previously to study single electron transfer events in surface-immobilized flavins and flavoenzymes, *e.g.* sarcosine oxidase, by direct wide-field imaging of ZMW arrays. Single molecule electron transfer dynamics have now been extended to the study of freely diffusing molecules using fluorescence measurements of Au ZMWs under single occupancy conditions. The Au in the ZMW serves both as an optical cladding layer and as the working electrode for potential control, thereby accessing single molecule electron transfer dynamics at μM concentrations. Consistent with expectations, the probability of observing single reduced molecules increases as the potential is scanned negative, $E_{appl} < E_{eq}$, and the probability of observing emitting oxidized molecules increases at $E_{appl} > E_{eq}$. Different single molecules exhibit different electron transfer properties as reflected in the position of E_{eq} and the distribution of E_{eq} among a population of FMN molecules. Two types of actively-controlled electroluminescence experiments were used: chronofluorometry experiments, in which the potential is alternately stepped between oxidizing and reducing potentials, and cyclic potential sweep fluorescence experiments, analogous to cyclic voltammetry, these latter experiments exhibiting a dramatic scan rate dependence with the slowest scan rates showing distinct intermediate states that are stable over a range of potentials. These states are assigned to flavosemiquinone species that are stabilized in the special environment of the ZMW nanopore.

[a]*Department of Chemistry and Biochemistry, University of Notre Dame, Notre Dame, IN 46556, USA. E-mail: pbohn@nd.edu*

[b]*Department of Chemical and Biomolecular Engineering, University of Notre Dame, Notre Dame, IN 46556, USA*

† These authors contributed equally to this work.

Introduction

Since the first single molecule electrochemical experiments were performed with electrochemiluminescence[1] and redox cycling,[2,3] interest in investigating single molecule electrochemistry, particularly by means of coupling fluorescence and electrochemistry, has increased. In this context, the use of fluorescence microscopy, particularly total internal reflectance fluorescence, with electrochemistry gives researchers a powerful tool in investigating redox chemistry at high spatial resolution, while simultaneously minimizing background interference.[4] Early applications of coupled fluorescence microscopy and electrochemistry targeted absorption at chemical interfaces and the development of new biosensors.[5–8] In these experiments, redox-sensitive optical properties – either the absorption cross-section, or the fluorescence quantum efficiency, or both – of the molecule were exploited to observe electron transfer events spectroscopically. The utility of coupling electrochemical measurements and fluorescence is evidenced by recent studies of redox cycling, catalyst screening and diffusion zone imaging.[9–12] A common feature of coupled electrochemical–luminescence experiments is that a current measurement, with the attendant large background, is replaced by the detection of luminescent photons – in principle a zero background measurement.

Bard and Barbara first extended coupled luminescence and electrochemical measurements to single molecule detection.[13–16] Distinct differences in single molecule fluorescence dynamics were observed at E_{appl} values above and below the equilibrium potential, E_{eq}, thereby firmly establishing fluorescence spectroscopy as a tool to monitor the dynamics of single electron transfer events. The systems initially investigated by single molecule electrochemical fluorescence spectroscopy were confined to molecular solids and immobilized molecules, but these systems were extended to single molecule spectroelectrochemical behaviour under diffusive conditions with studies of cresyl violet[17,18] and other electrochemically active fluorophores.[19–26] Redox switching of single protein molecules has been investigated by observing the resonance energy transfer between the Cu redox center and covalently-linked Cy5 dye in the blue Cu protein azurin, the resulting studies yielding reaction kinetics and thermodynamic dispersion.[27–29] Previous work from this laboratory has exploited nanophotonic architectures, specifically zero-mode waveguides (ZMW) to investigate homogeneous electron transfer dynamics of sarcosine oxidase, both with its nominal substrate, *N*-methylglycine (sarcosine) as well as a non-canonical substrate, L-proline.[30] These experiments were extended to the use of the optical cladding layer of the ZMW as the working electrode in a spectroelectrochemical cell in studies of surface-functionalized flavin adenine dinucleotide (FAD).[31] Flavins are of particular interest, since they function as cofactors in many important enzymes, especially among the oxidoreductases.

Single molecule spectroscopy generally requires reducing the observation volume by means such as total internal reflection or tightly focused excitation in order to maximize the signal-to-background ratio and to produce reasonable signal magnitudes at single molecule levels.[32,33] More recently, single molecule experiments have been implemented by trapping molecules in nanophotonic architectures, such as ZMWs. These are usually realized physically as an array of metal-clad nanopores, which do not support any far-field propagating modes

when the wavelength is greater than a critical wavelength $\lambda_c \sim 1.7d$, where d is the pore diameter.[34] Under these conditions an evanescent field is contained within the pore,[35,36] with a magnitude that decays exponentially along the longitudinal axis of the pore, of

$$I(z) = \frac{e^{-z}}{\Lambda} \tag{1}$$

where Λ is the decay constant and z is the distance in the pore. The decay constant is defined as

$$\frac{1}{\Lambda} = 2\left[\left(\frac{1}{\lambda_c}\right)^2 + \left(\frac{1}{\lambda_m}\right)^2\right]^{\frac{1}{2}} \tag{2}$$

where λ_m is the wavelength in the ZMW medium. The sharp decay of the evanescent field produces extremely small effective sampling volumes, V_{eff},[34,37] given by

$$V_{eff} = \frac{\pi d^2 \Lambda}{24} \tag{3}$$

Fabricating pores below 100 nm in diameter creates effective volumes $V_{eff} \sim$ 100 zL at 458 nm excitation in water. Utilizing pore volumes of this magnitude allows single molecule experiments to be conducted at relatively high concentrations. For example, at $V_{eff} \sim 100$ zL, single molecule occupancy is reached at a concentration $C \sim 17$ μM.

Zero-mode waveguides have been utilized for measurements of single enzyme kinetics, membrane diffusion, protein interactions, and a variety of other detailed studies at the single molecule level.[34,38–41] Generally, Al with its short skin depth is the metal of choice for the cladding layer in ZMW structures. Previously, our laboratory utilized Au-clad ZMWs due to the ability of Au to function as a working electrode (large ideally polarizable region), the wide range of thiol-based surface chemistries available to functionalize molecules to the Au surface, and the chemical orthogonality of Au and SiO_2, the common base material for ZMW supports.[42] Thus, Au can provide multi-functional utility, serving simultaneously as both the optical blocking layer of the ZMW and the working electrode of an electrochemical cell, a dual functionality that is at the heart of the work reported here.

Flavin mononucleotide, FMN, was chosen for detailed spectroelectrochemistry studies under single occupancy conditions (*i.e.* solution conditions where the expectation value for the ZMW nanopore occupancy ranges from ~0.13 to 1.3). FMN contains an isoalloxazine chromophore that is fluorescent in the oxidized state, while the reduced state, $FMNH_2$, exhibits dramatically lower light emission, characteristic of a dark-state. Intriguingly, FMN has a relatively constant fluorescence quantum efficiency over a large pH window, but the electrochemical behaviour varies significantly with pH.[43,44] These properties, coupled with the intrinsic biochemical relevance as important cofactors in flavoenzymes, make the flavins ideal candidates for monitoring single molecule fluorescence under active electrochemical potential control in a redox-active ZMW. FMN was chosen over flavin adenine dinucleotide, FAD, since the presence of the adenine base

significantly complicates the radiative dynamics in free solution.[45] Au ZMWs were used to study freely diffusing, rather than immobilized, FMN/$FMNH_2$ using both statically and actively-controlled voltage programs. Constant potential experiments show strong correlation between E_{appl} and fluorescence intensity at the single molecule occupancy level, while potential step experiments (chronofluorometry) and cyclic potential sweep fluorescence (CPSF), are utilized to examine the coupling between single molecule transport and electron transfer in the ZMW nanopores.

Experimental

ZMW fabrication

ZMWs were fabricated as previously described.[30,31] Briefly, 5 nm of Ti and 200 nm of Au were deposited by electron beam evaporation on coverslips (no. 1.5H, Schott). Focused ion beam (FIB) milling was used to create the ZMW. The pores were milled at 9.7 pA with a dwell time of 0.1 ms. Typically, 11 × 11 arrays were fabricated with 4 large pores at the corners to assist in locating the ZMW array prior to single molecule experiments. The device was then cleaned with 1.0 M KOH at 80 °C for 45 min followed by 10 min in concentrated H_2SO_4 and 10 min in concentrated HNO_3. A PDMS well was affixed to the device though plasma bonding to hold solution over the area occupied by the ZMWs.

Finite element simulations

The numerical calculations are performed with a finite element method using COMSOL Multiphysics version 4.4. The simulation was performed over a two-dimensional domain representing the geometry and dimensions of the zero-mode waveguides employed in our experiments. The zero-mode waveguide is represented by a single pore consisting of a conical compartment. The geometry is adapted from scanning electron micrographs (SEMs) of FIB cross-sections. The domain above the single pore was drawn sufficiently large to avoid interference from boundaries, and the mesh was refined both within the single pore and in the region just above the single pore to provide sufficient resolution.

Electrochemical measurements

Electrochemical measurements were performed using a potentiostat (750E, CH Instruments). Both bulk and nanopore measurements made under single occupancy conditions were performed with a Pt counter electrode and a Ag/AgCl reference electrode. Bulk electrochemical measurements used a 3 mm Au disk working electrode (WE), and nanopore measurements used the Au ZMW array as the WE. Electrical contact to the ZMW was made at an exposed tab away from the ZMW area.

Fluorescence Measurements

A custom-built confocal microscope was used to collect all fluorescence data. 458 nm radiation from a continuous wave laser (Sapphire 458 LP, Coherent) was passed through a spatial filter to select the TEM_{00} mode and then a quarter wave plate to produce circularly polarized light. A dichroic filter (Z488RDC, Chroma Technology Corporation) reflected the collimated beam into the back aperture of

a 40×, 1.30 NA oil immersion objective (420260-9900-000, Carl Zeiss, Inc.) to produce a diffraction-limited spot with 40 μW power at the focal plane. Fluorescence emission was collected by the same objective (epi-fluorescence) and passed through three emission filters (ET500lp, ET525/50m, ET500lp, Chroma Technology Corporation) before being focused through a 30 μm diameter confocal pinhole to define the radiation for a single-photon avalanche photodiode detector (SPCM-AQR-16, Perkin-Elmer, Inc.). A hardware correlator (TimeHarp260 PICO Single, PicoQuant) was used to collect single molecule fluorescence data. The fluorescence optical path was augmented with a trans-illumination path to assist in locating the ZMW pores. To access the trans-illumination path, collimated radiation from a 632.8 nm laser was used to illuminate the back surface of the ZMW array. Radiation emerging from the pores was collected by the objective, and a mirror was rotated into the detection path to deflect the transmitted radiation to a video-rate CCD camera (JE7462DC, Javelin Systems). Once located, the pore array was indexed to the motion of a piezoelectric stage (P-517.2CL, Physik Instrumente) to reliably center the x–y focal position of the objective on the ZMW pore of interest.

Results and discussion

Evanescent field attenuation and fabrication of ZMW working electrodes

11 × 11 square ZMW arrays of variable pitch (5 μm, typ.) were fabricated in Au to produce a working electrode array capable of supporting the optical and electrochemical requirements of spectroelectrochemistry under single molecule occupancy conditions. Despite having a smaller skin depth than Al, Au was chosen for the optical cladding layer due to its large ideally polarizable region, and ZMWs were designed and fabricated to effectively confine the optical field and reduce the active volume. As Fig. 1 illustrates, larger pores were FIB milled into the corners of the ZMW array as optical reference marks to assist in the location of the ZMW nanopores using trans-illumination. FIB direct writing of ZMWs produces pores with conical frustum shapes rather than the cylindrical shapes obtained using electron beam lithography to produce ZMW arrays. The SEMs and schematic diagram in Fig. 1 show a cross-section of a typical single ZMW nanopore, illustrating the conical pore cross-section as well as the overetched region, which is a common feature of pores produced by FIB milling.[30] The overetched region past the Au/glass interface is typically the same width as the pore bottom diameter (d_{bottom}) and well-controlled milling processes yield overetch depths less than 50 nm.

The evanescent field decays exponentially with distance in cylindrical pores at a rate that depends on the radius and diameter. To assess the behavior in the conical ZMW nanopores studied here, finite element simulations were performed at various conical frustum sizes and geometries. Fig. 2 shows the electric field in a series of conical frustum pores each having a ratio of top diameter, d_{top}, to bottom diameter, d_{bottom}, $d_{\mathrm{top}}/d_{\mathrm{bottom}} = 2$. As Fig. 2 illustrates, the field decays exponentially, and the nanostructures provide excellent attenuation, primarily determined by d_{bottom}. Structures fabricated for this study generally had $d_{\mathrm{top}} \sim 80$–125 nm, and $d_{\mathrm{bottom}} \sim 20$–$60$ nm with $d_{\mathrm{top}} : d_{\mathrm{bottom}}$ ratios between 1.5 and 4.0. At positions in the pore exhibiting attenuations in excess of $1/e^2$, the evanescent field strength is likely insufficient for excitation of fluorescence. The exact position in

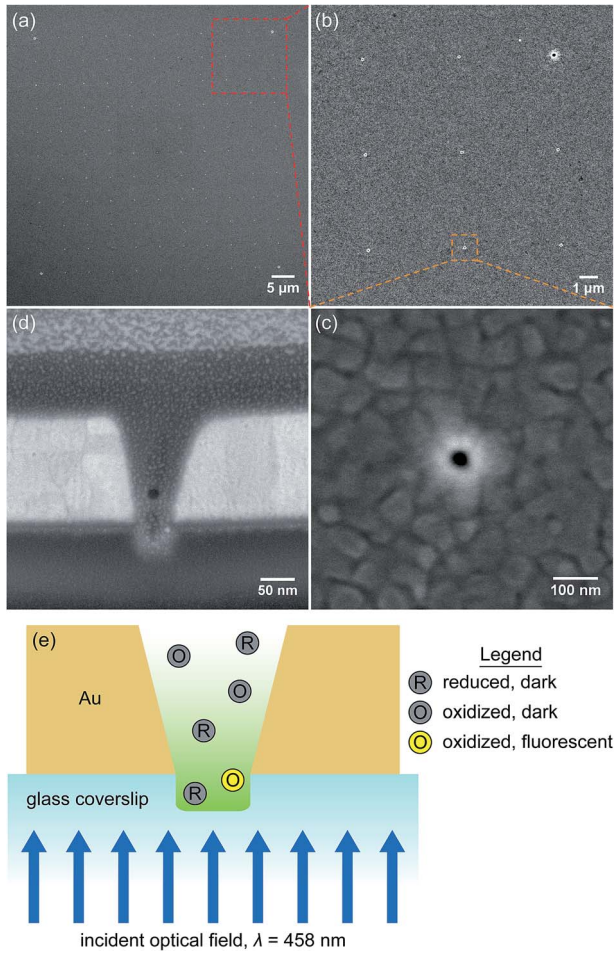

Fig. 1 Scanning electron micrographs of a ZMW array at different magnifications and perspectives: (a) top-down view of the entire 11 × 11 ZMW array, (b) top-down view of a 3 × 3 subset of the same array, (c) top-down view of a single nanopore with $d \sim 40$ nm, and (d) cross-section of a nanopore filled with Pt to assist imaging. (e) Schematic illustration of an over-etched ZMW with reduced and oxidized FMN molecules shown freely diffusing.

the pore at which the attenuation exceeds $1/e^2$ varies with pore diameter and shape, so the effective volume, where the majority of excitation/emission events occur, is typically constrained to the bottom 5–20% of the pore.

One of the advantages of using nanophotonic ZMWs is the extremely small effective sampling volume. Fig. 3 shows how the effective volume depends on d_{bottom} at $d_{\text{top}} : d_{\text{bottom}}$ values of 1.5, 2.0, and 3.0. The effective volumes for different pore shapes deviate from each other only at large d_{bottom} values. In addition, the concentration required to achieve a molecular occupancy expectation value of 1, *i.e.* $\langle N \rangle = 1$, is also shown as a function of d_{bottom}. Based on the simulations shown in Fig. 2 and taking into account the volume of the overetched region, the total effective volumes of the ZMWs used in this study are

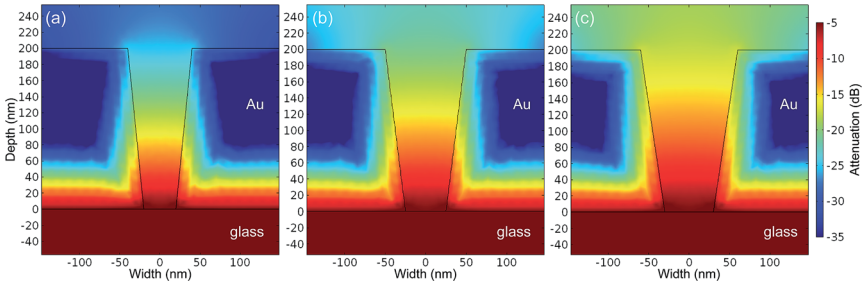

Fig. 2 Cross-sectional heat maps of evanescent field amplitudes in conical nanopores obtained by finite element simulations, showing attenuation as a function of nanopore geometry. All three structures exhibit $d_{top} : d_{bottom} = 2$, and $d_{bottom} =$ (a) 40 nm, (b) 50 nm, and (c) 60 nm.

approximately 200 zL, assuming that the volumes of the metal-enclosed pore and the overetched region are roughly equal. At this volume, molecular occupancies of $\langle N \rangle = 1.2$ and $\langle N \rangle = 0.12$ are expected at 10 and 1 μM, respectively. Additionally, Monte-Carlo simulations of Brownian motion were performed on the conical nanopore geometries of relevance in these experiments. In these simulations, the mean residence time, defined as the time it takes for a randomly positioned particle to diffuse out of the effective volume of the pore, is calculated to be in the range ~0.5 to 3.5 μs depending on pore geometry.

Statically coupled fluorescence and electrochemistry

Initial experiments were implemented to characterize the emission rates of freely diffusing FMN molecules under static control of potential values in the range $E_{appl} = +0.06$ V to -0.44 V at FMN formal concentrations of 10 μM and 1 μM, where the average molecular occupancy is $\langle N \rangle = 1.2$ and 0.12 molecules, respectively. Solutions were held at constant potential for ~30 s in order to ensure that steady state was reached at the ZMW electrode, after which the fluorescence signal was recorded. Histograms of the signal intensities were then fit to Poisson functions

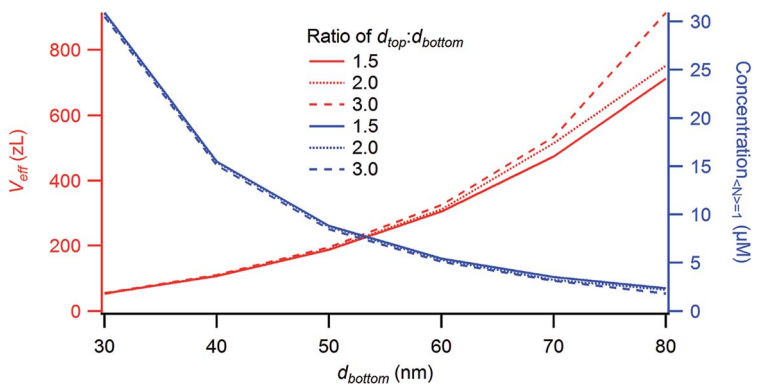

Fig. 3 Effective volumes (left ordinate) and concentrations for single molecule occupancy (right ordinate) for $d_{top} : d_{bottom}$ ratios of 1.5, 2.0, and 3.0 as a function of d_{bottom}.

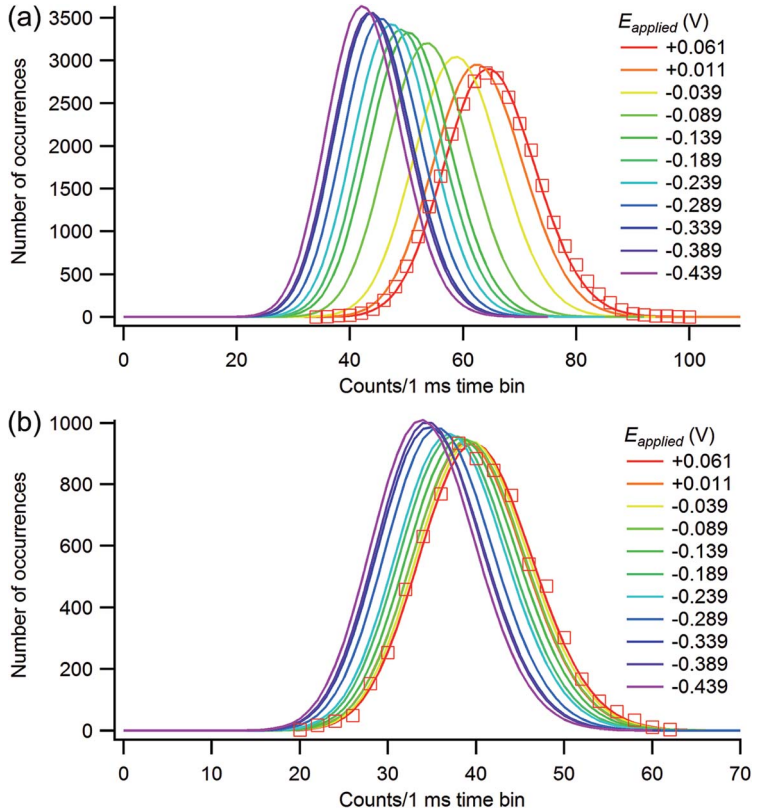

Fig. 4 Poisson distribution fits to histograms of fluorescence intensities at different values of E_{appl} for (a) 10 μM and (b) 1 μM FMN in 100 mM citrate buffer at pH 2.9. Experimental data are included with the fit for $E_{appl} = +0.061$ V to illustrate the quality of the fit.

to produce the distributions shown in Fig. 4. At both average occupancy levels, the distribution shifts to higher intensity values as the potential is made more positive, consistent with the molecules being more likely to be in the oxidized state; FMN is shown in Scheme 1.

With the potential poised at the most positive value, $E_{appl} = +0.06$ V, the peak of the fluorescence emission distribution occurs at $I_{ox} \sim 64$ ms^{-1}, while at the most negative value, $E_{appl} = -0.44$ V, the fluorescence signal decreases to $I_{red} \sim 41$ ms^{-1}. The intensity observed at oxidizing potentials is consistent with estimates of the emission rate for FMN excited at 458 nm based on single molecule occupancy, the measured irradiance at the ZMW array, and the estimated collection efficiency. However, the "dark state" emission observed at $E_{appl} = -0.44$ V is significantly higher than the apparent emission level, $I_{bkgnd} \sim 3$ ms^{-1}, observed in the absence of fluorophore in control experiments. The latter observation can be understood by considering three dynamic processes: (1) the intrinsic photopumping and luminescence dynamics of the fluorophore, (2) transport of both oxidized and reduced molecules into and out of the ZMW nanopore, and (3) heterogeneous electron transfer at the Au cladding/working electrode. The intrinsic photopumping and emission dynamics are

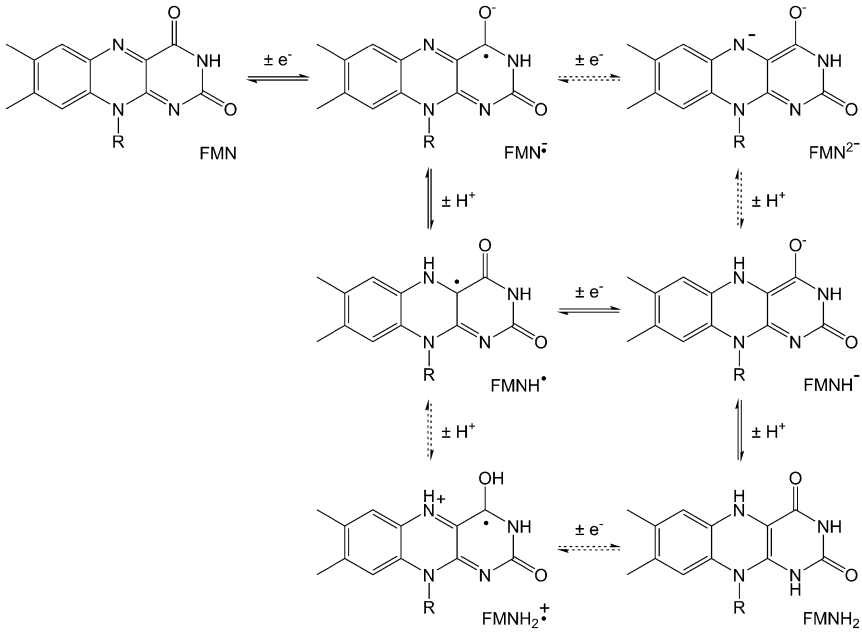

Scheme 1

overwhelmingly associated with the oxidized state, so the most likely explanation for the observation that $I_{red} > I_{bkgnd}$ involves occupancy of the ZMW nanopore by oxidized FMN under nominally reducing conditions, and the FMN can arise from two sources. Since the experiment begins with oxidized FMN, there is always a background population of fluorescent species that can diffuse into the excitation volume. In addition, $FMNH_2$ may react with dissolved O_2 in the nanopore to produce FMN, independent of the potential on the electrode. Some of these FMN molecules will diffuse to the Au surface and be reduced prior to diffusing out of the pore, so the level of emission observed at I_{red} likely reflects the balance between new oxidized species entering, or being generated in, the pore and oxidized species being reduced while in the ZMW. Since the time bin for data collection (1 ms) is $\geq 300\times$ the average residence time obtained from Monte-Carlo simulations, there is ample time to sample many individual molecules during the collection window.

The other interesting feature of these data concerns the narrowing of the intensity distribution at lower concentration. When the static potential experiment is repeated at [FMN] = 1 μM (Fig. 4(b)) the distribution shifts to higher intensity values, as the potential is made more positive, just as with the higher concentration, but the spread of fluorescence intensity distributions is considerably narrower. The negative end of the distribution decreases to $I_{red} \sim 34\ ms^{-1}$, but the positive end at $E_{appl} = +0.06$ V has a maximum at $I_{ox} \sim 40\ ms^{-1}$. The narrowed distribution is also consistent with the putative mechanism for I_{bkgnd} advanced above, as the lower concentration would be expected to yield a smaller departure from the background simply due to the smaller number of reduced species capable of diffusing into the ZMW.

Dynamics of coupled fluorescence and electrochemistry

Having established the conditions under which single molecule occupancy is achieved in ZMWs, the optimum geometries for coupling optical radiation into solutions supporting single redox-active molecules in close proximity to a working electrode, and the static potential dependence of FMN emission from ZMWs, the next fluorescence measurements were made under active potential control to explore how electrochemistry couples to a population of freely diffusing single molecules. Fig. 5 shows a comparison of the potential dependence of FMN luminescence from a single ZMW nanopore obtained at [FMN] = 10 μM in 100 mM pH 2.9 citrate buffer to a bulk measurement of the cyclic voltammetry (CV) for 5 mM FMN in the same buffer. At pH 2.9, the half-wave potential of FMN, determined from CV at [FMN] = 5 mM, is $E_{1/2} = -0.19$ V *vs.* Ag/AgCl. Furthermore, even though the luminescence data are acquired in a very different physical environment, the inflection in the potential-dependent luminescence curve is in reasonable agreement with the bulk electrochemical value.

A single molecule occupancy chronofluorometry experiment is shown in Fig. 6. Analogous to the more familiar chronoamperometry, this experiment monitors the fluorescence, as opposed to the current, response of a redox system to alternating potential steps. Given the $E_{1/2} = -0.19$ V determined for FMN in Fig. 5, the chronofluorometry experiment was designed to step between ±0.25 V overpotentials *vs.* Ag/AgCl ($E_{appl} = +0.06$ V and -0.44 V) in order to produce conditions in which FMN alternates between the fully oxidized and fully reduced states, represented in Scheme 1 as FMN and $FMNH_2$, the latter being the fully protonated form of reduced FMN, appropriate to experiments at pH 2.9. Although both longer and shorter time windows were investigated, the 5 s potential steps used in Fig. 6 are sufficiently long to allow the system to achieve steady state at both oxidizing and reducing conditions.

Clearly, the fluorescence response in Fig. 6 is strongly correlated to the applied potential steps. The experiment is initiated at an oxidizing potential, and stepping

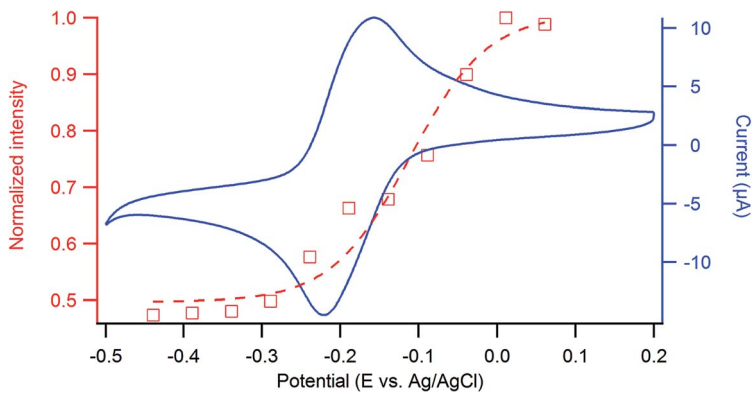

Fig. 5 Comparison of the potential dependence of FMN luminescence (discrete data points) from a single ZMW nanopore obtained at [FMN] = 10 μM in 100 mM pH 2.9 citrate buffer to a bulk measurement of the cyclic voltammetry for 5 mM FMN in the same buffer (solid curve). The dashed line gives the fit of the luminescence data to a sigmoidal optical response function.

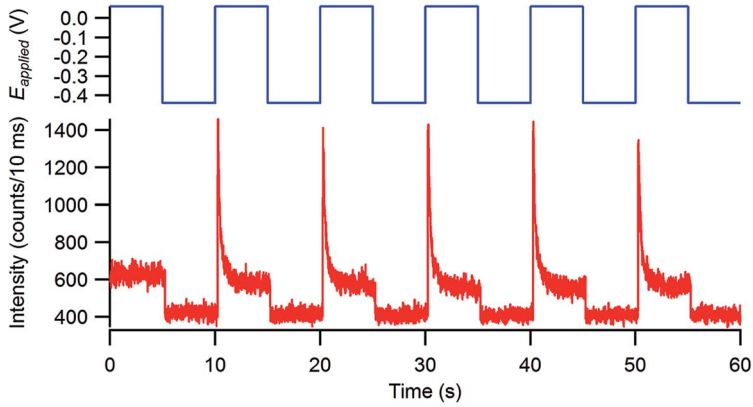

Fig. 6 Chronofluorometry of 10 μM FMN in 100 mM citrate buffer at pH 2.9. The potential (*vs.* Ag/AgCl) is modulated at 5 s intervals between 0.06 V and −0.44 V, and fluorescence emission is monitored from a single $d_{top} = 80$ nm, $d_{bottom} = 40$ nm ZMW nanopore using 10 ms time bins.

to a reducing potential causes an immediate decrease in emission intensity from ~64 ms^{-1} to ~41 ms^{-1}, consistent with the steady-state values shown in Fig. 4. Interestingly, when the potential is returned to an oxidizing value, the fluorescence signal exhibits a significant and reproducible positive transient before decaying to the steady state value $I_{ox} \sim 64$ ms^{-1}, a transient not observed in Fig. 4, because the static potential results were obtained at steady-state. Because the potential step occurs rapidly compared to molecular transport, any reduced molecules in the nanopore would be oxidized within the time required to diffuse to the pore wall; $\tau_{diff} \sim 1.5$ μs for a 60 nm diameter pore and $D \sim 10^{-6}$ cm^2 s^{-1}, thus establishing a momentarily larger population of oxidized FMN in and near the ZMW pores. This augmented population would be responsible for the initial increase in fluorescence observed on the positive potential step, after which a return to a steady-state population would be established by the balance between diffusion of FMN into the pore and oxidation of $FMNH_2$, against diffusion of FMN out of the pore and perhaps other processes, such as photobleaching, which would decrease the population of fluorescent species in and near the ZMW nanopore.

The single molecule occupancy fluorescence analog of the cyclic voltammetry experiments is shown in Fig. 7 at three distinct scan rates. At the fastest scan rate, 0.5 V s^{-1}, the luminescence behavior of 10 μM FMN is similar to that expected from a bulk measurement. As shown in Fig. 7(a), the fluorescence response is symmetric and reproducible, oscillating between extreme values of $I_{ox} \sim 70$ ms^{-1} and $I_{red} \sim 43$ ms^{-1}, similar to the results obtained at static potentials and with chronofluorometry. Decreasing the scan rate to 50 mV s^{-1}, the response develops an asymmetric shape, *cf.* Fig. 7(b), with a shoulder on the negative-going scan and a constant intensity observed over an extended window of reducing potentials. Finally, at the slowest scan rate studied, 1 mV s^{-1}, *cf.* Fig. 7(c), the potential-dependent fluorescence develops distinct additional states with fluorescence emission intensities $I_{int} \sim 32$ ms^{-1} intermediate between the values $I_{ox} \sim 44$ ms^{-1} and $I_{red} \sim 25$ ms^{-1}.

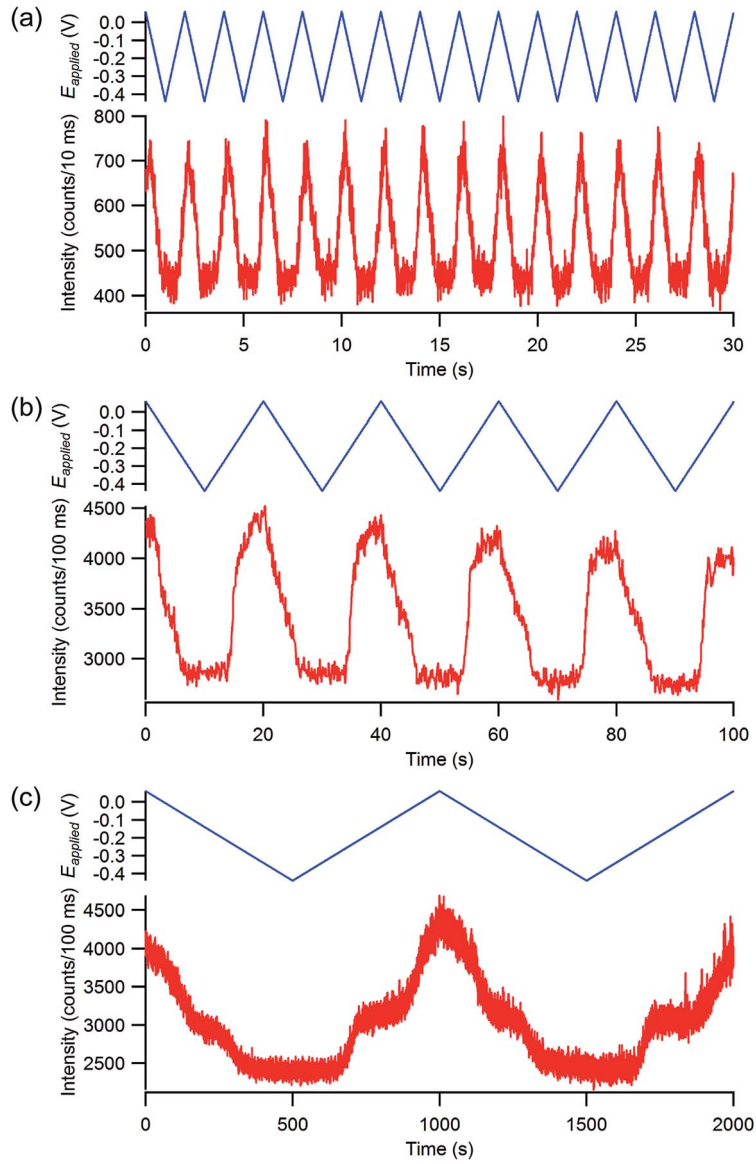

Fig. 7 Cyclic potential sweep fluorescence measurements of 10 μM FMN in 100 mM citrate buffer at pH 2.9 at scan rates of (a) 0.5 V s^{-1}, (b) 0.05 V s^{-1}, and (c) 0.001 V s^{-1}. In each panel, the potential program is shown at the top, and the fluorescence response at the bottom.

The asymmetric fluorescence potential response at 50 mV s^{-1} and the intermediate emission intensity states observed at 1 mV s^{-1} are likely due to intermediate reaction steps between FMN and $FMNH_2$. Scheme 1 shows all of the reaction pathways by which proton-coupled electron transfer can connect the fully oxidized FMN to the fully reduced (and protonated) $FMNH_2$, with the preferred pathway at pH 2.9 indicated by the solid equilibrium symbols. However,

in the most general view at least three possible reaction pathways exist, with 5 possible intermediates including 3 semiquinones.[46] At pH 2.9 the reduction of FMN to $FMNH_2$ is thought to occur through two separate proton-coupled ($1e^-$/$1H^+$) steps through an intermediate flavosemiquinone ($FMNH^\bullet$ in Scheme 1) that is stabilized in the flavoprotein environment. In contrast, flavosemiquinone species are observed to undergo rapid dismutation in bulk solution. Thus, the appearance of a stable intermediate species in the slow cyclic potential sweep experiment suggests that the special environment of the ZMW nanopore facilitates the stabilization of the flavosemiquinone species, a behavior of radical redox species that is not observed in bulk solution.

Conclusions

ZMWs fabricated with Au cladding layers are attractive substrates for investigating electrofluorogenic behavior of freely diffusing single molecules. The combination of the small volume ($V_{eff} \sim 200$ zL) and the efficient confinement of optical radiation in the conical FIB-milled ZMW nanopores used here make it possible to study the electroluminescence behavior of single flavin ($FMN/FMNH_2$) molecules under both static and active potential control. Under static potential control fluorescence intensity histograms are consistent with expectations based on bulk studies, *i.e.* fluorescence increases as E_{appl} becomes more positive. However, a non-zero luminescence intensity is observed even at the most negative applied potentials, an observation that is ascribed to the interplay between the transport of oxidized and reduced molecules into and out of the ZMW nanopore and redox reactions at the Au cladding/working electrode.

Two types of actively-controlled electroluminescence experiments were performed at the single molecule occupancy level in these structures: chronofluorometry experiments, in which the potential is alternately stepped between oxidizing and reducing potentials, and fluorescence-reported cyclic potential sweep experiments, the fluorescence analog of cyclic voltammetry. Chronofluorometry measurements exhibit a fluorescence response that is strongly correlated to applied potential steps, but with an interesting asymmetry between the negative- and positive-going steps. The substantial fluorescence transient observed on the positive-going step is attributed to an augmented population of oxidized species that is depleted over time by diffusion of FMN out of the pore and possibly also by photobleaching. Fluorescence-reported cyclic potential sweep experiments under single occupancy conditions exhibit a dramatic scan rate dependence with the slowest scan rates showing distinct intermediate states that are stable over a range of potentials. These states are tentatively assigned to flavosemiquinone species that are stabilized in the special environment of the ZMW nanopore. The ultra-small volume and efficient trapping of optical fields in the ZMW nanopores makes these systems attractive platforms for future single molecule and single enzyme spectroelectrochemical investigations.

Acknowledgements

This work was supported by the National Science Foundation under grant NSF1404744 (LPZ) and the Department of Energy Office of Science under grant DE FG02 07ER15851 (DAG) and a subcontract from Oak Ridge National Laboratory

(DH). Fabrication and structural characterization of the devices studied here were accomplished at the Notre Dame Nanofabrication Facility and the Notre Dame Integrated Imaging Facility, respectively, whose generous support is gratefully acknowledged. We thank David Heemstra of Notre Dame Nanofabrication Facility for useful advice on fabrication procedures.

References

1 M. M. Collinson and R. M. Wightman, *Science*, 1995, **268**, 1883–1885.
2 F. R. F. Fan and A. J. Bard, *Science*, 1995, **267**, 871–874.
3 F. R. F. Fan, J. Kwak and A. J. Bard, *J. Am. Chem. Soc.*, 1996, **118**, 9669–9675.
4 P. Audebert and F. Miomandre, *Chem. Sci.*, 2013, **4**, 575–584.
5 M. A. Jones and P. W. Bohn, *Anal. Chem.*, 2000, **72**, 3776–3783.
6 M. A. Jones and P. W. Bohn, *J. Phys. Chem. B*, 2001, **105**, 2197–2204.
7 F. Miomandre, E. Lepicier, S. Munteanu, O. Galangau, J. F. Audibert, R. Meallet-Renault, P. Audebert and R. B. Pansu, *ACS Appl. Mater. Interfaces*, 2011, **3**, 690–696.
8 F. Miomandre, R. Meallet-Renault, J. J. Vachon, R. B. Pansu and P. Audebert, *Chem. Commun.*, 2008, 1913–1915.
9 C. Ma, L. P. Zaino and P. W. Bohn, *Chem. Sci.*, 2015, **6**, 3484–3491.
10 Y. Fu, J. Zhang and J. R. Lakowicz, *Langmuir*, 2008, **24**, 3429–3433.
11 J. P. Guerrette, S. J. Percival and B. Zhang, *J. Am. Chem. Soc.*, 2013, **135**, 855–861.
12 S. M. Oja, J. P. Guerrette, M. R. David and B. Zhang, *Anal. Chem.*, 2014, **86**, 6040–6048.
13 R. E. Palacios, F. R. F. Fan, A. J. Bard and P. F. Barbara, *J. Am. Chem. Soc.*, 2006, **128**, 9028–9029.
14 Y. L. Chang, R. E. Palacios, F. R. F. Fan, A. J. Bard and P. F. Barbara, *J. Am. Chem. Soc.*, 2008, **130**, 8906–8907.
15 R. E. Palacios, F. R. F. Fan, J. K. Grey, J. Suk, A. J. Bard and P. F. Barbara, *Nat. Mater.*, 2007, **6**, 680–685.
16 R. E. Palacios, W. S. Chang, J. K. Grey, Y. L. Chang, W. L. Miller, C. Y. Lu, G. Henkelman, D. Zepeda, J. Ferraris and P. F. Barbara, *J. Phys. Chem. B*, 2009, **113**, 14619–14628.
17 C. H. Lei, D. H. Hu and E. J. Ackerman, *Chem. Commun.*, 2008, 5490–5492.
18 C. H. Lei, D. H. Hu and E. Ackerman, *Nano Lett.*, 2009, **9**, 655–658.
19 C. M. Hill, D. A. Clayton and S. Pan, *Phys. Chem. Chem. Phys.*, 2013, **15**, 20797–20807.
20 J. Liu, C. M. Hill, S. L. Pan and H. Y. Liu, *Phys. Chem. Chem. Phys.*, 2014, **16**, 23150–23156.
21 H. Shen, W. L. Xu and P. Chen, *Phys. Chem. Chem. Phys.*, 2010, **12**, 6555–6563.
22 G. Zhang, L. Xiao, R. Chen, Y. Gao, X. Wang and S. Jia, *Phys. Chem. Chem. Phys.*, 2011, **13**, 13815–13820.
23 A. J. Bard, *ACS Nano*, 2008, **2**, 2437–2440.
24 S. G. Lemay, S. Kang, K. Mathwig and P. S. Singh, *Acc. Chem. Res.*, 2013, **46**, 369–377.
25 K. Mathwig, T. J. Aartsma, G. W. Canters and S. G. Lemay, *Annu. Rev. Anal. Chem.*, 2014, **7**, 383–404.

26 J. M. Salverda, A. V. Patil, G. Mizzon, S. Kuznetsova, G. Zauner, N. Akkilic, G. W. Canters, J. J. Davis, H. A. Heering and T. J. Aartsma, *Angew. Chem., Int. Ed.*, 2010, **49**, 5776–5779.
27 N. Akkilic, F. v. d. Grient, M. Kamran and N. J. M. Sanghamitra, *Chem. Commun.*, 2014, **50**, 14523–14526.
28 A. V. Patil and J. J. Davis, *J. Am. Chem. Soc.*, 2010, **132**, 16938–16944.
29 N. Akkilic, M. Kamran, R. Stan and N. Sanghamitra, *Biosens. Bioelectron.*, 2015, **67**, 747–751.
30 J. Zhao, S. P. Branagan and P. W. Bohn, *Appl. Spectrosc.*, 2012, **66**, 163–169.
31 J. Zhao, L. P. Zaino and P. W. Bohn, *Faraday Discuss.*, 2013, **164**, 57–69.
32 E. Haustein and P. Schwille, *Annu. Rev. Biophys.*, 2007, **36**, 151–169.
33 W. E. Moerner and D. P. Fromm, *Rev. Sci. Instrum.*, 2003, **74**, 3597–3619.
34 M. J. Levene, J. Korlach, S. W. Turner, M. Foquet, H. G. Craighead and W. W. Webb, *Science*, 2003, **299**, 682–686.
35 H. A. Bethe, *Phys. Rev.*, 1944, **66**, 163–182.
36 C. J. Bouwkamp, *Philips Res. Rep.*, 1950, **5**, 321–332.
37 J. M. Moran-Mirabal and H. G. Craighead, *Methods*, 2008, **46**, 11–17.
38 J. Korlach, M. Levene, M. Foquet, S. W. Turner, H. G. Craighead and W. W. Webb, *Biophys. J.*, 2003, **84**, 141A.
39 J. Korlach, M. Levene, S. W. Turner, H. G. Craighead and W. W. Webb, *Biophys. J.*, 2002, **82**, 507A.
40 P. Zhu and H. G. Craighead, *Annu. Rev. Biophys.*, 2012, **41**, 269–293.
41 K. T. Samiee, J. M. Moran-Mirabal, Y. K. Cheung and H. G. Craighead, *Biophys. J.*, 2006, **90**, 3288–3299.
42 C. D. Kinz-Thompson, M. Palma, D. K. Pulukkunat, D. Chenet, J. Hone, S. J. Wind and R. L. Gonzalez, *ACS Nano*, 2013, **7**, 8158–8166.
43 S. D. M. Islam, T. Susdorf, A. Penzkofer and P. Hegemann, *Chem. Phys.*, 2003, **295**, 137–149.
44 A. Sengupta, R. V. Khade and P. Hazra, *J. Photochem. Photobiol., A*, 2011, **221**, 105–112.
45 Y. T. Kao, C. Saxena, T. F. He, L. J. Guo, L. J. Wang, A. Sancar and D. P. Zhong, *J. Am. Chem. Soc.*, 2008, **130**, 13132–13139.
46 S. L. J. Tan, J. M. Kan and R. D. Webster, *J. Phys. Chem. B*, 2013, **117**, 13755–13766.